The effects of space charge, dopants, and strain fields on surfaces and grain boundaries in YBCO compounds

Haibin Su[1,3] and David O Welch[2]

[1] Department of Materials Science and Engineering, SUNY at Stony Brook, Stony Brook, NY 11794, USA

[2] Department of Materials Science, Brookhaven National Laboratory, Upton, NY 11973, USA

[3] Present address: Beckman Institute 139-74, California Institute of Technology, Pasadena, CA 91125, USA

E-mail: hbsu@wag.caltech.edu and dwelch@bnl.gov

Abstract

Statistical thermodynamical and kinetically-limited models are applied to study the origin and evolution of space charges and band-bending effects at low-angle [001] tilt grain boundaries in $YBa_2Cu_3O_7$ and the effects of Ca doping upon them. Atomistic simulations, using shell models of interatomic forces, are used to calculate the energetics of various relevant point defects. The intrinsic space charge profiles at ideal surfaces are calculated for two limits of oxygen contents, i.e. $YBa_2Cu_3O_6$ and $YBa_2Cu_3O_7$. At one limit, O_6, the system is an insulator, while at O_7 it is a metal. This is analogous to the intrinsic and doping cases of semiconductors. The site selections for doping calcium and creating holes are also investigated by calculating the heat of solution. In a continuum treatment, the volume of formation of doping calcium at Y-sites is computed. It is then applied to study the segregation of calcium ions to grain boundaries in the Y-123 compound. The influences of the segregation of calcium ions on space charge profiles are finally studied to provide one guide for understanding the improvement of transport properties by doping calcium at grain boundaries in the Y-123 compound.

1. Introduction

The study of grain boundaries of YBCO is very important, because they act as strong barriers to current flow in YBCO [1]. This behaviour of high temperature superconductors is in sharp contrast to low temperature superconductors, in which grain boundaries are not only transparent to current, but also significantly contribute to flux pinning. The formation of such weak links in high temperature superconductors is due to the low carrier density and strong dependence of T_c on hole concentration. There are many experiments showing that the critical current density through grain boundaries is very sensitive to the orientation of the adjacent

crystallites [2, 3].

Generally, a large misorientation angle will reduce J_c significantly. As we know, there are quite rich phenomena occurring in grain boundaries: variations in the chemical stoichiometry, dissociation of grain boundary dislocations, impurity segregation, etc. For instance, recently Kung *et al* [4] reported that small-angle [001] tilt grain boundaries in YBCO with (110) planes exhibit partial grain boundary dislocations separated by stacking faults. The dissociated grain boundary structures have twice the number of grain boundary dislocations and shorter interdislocation core channel widths than Frank's geometry rule predicts (in Frank's rule the separation between dislocations of small-angle θ boundaries is proportional to b/θ). This requires further development of the above model of supercurrent flow through arrays of small-angle grain boundaries. Furthermore, the situation gets more complicated because grain boundaries can also act as sinks and sources for vacancies. In ionic solids this can give rise to charging effects. The existence of space charge regions near free surfaces in an ionic solid was first postulated by Frenkel [5]. In an ionic solid, the vacancy concentrations at surfaces and grain boundaries are determined by the individual free energy of formation. The cation and anion vacancies usually have different formation energies. However, the vacancy concentrations in the bulk are determined by the condition of charge neutrality and usually they are different from those at the grain boundaries where strict charge neutrality conditions are relaxed. Thus, the vacancy concentration changes as a function of distance from the grain boundaries. Usually, vacancies in ionic solids are charged defects. Spatial distributions of these charged defects lead to a potential difference between the bulk and free surfaces and grain boundaries [6–9]. There are two kinds of space charges. Here we define a space charge arising from differences in point defect formation energies as an 'intrinsic space charge' to contrast with those due to segregated dopants and grain boundary nonstoichiometries.

The topic of space charges at interfaces arising from point defects has not been investigated so far for cuprates. Since holes carry a charge, it is expected that a space charge will produce a significant effect on hole distributions around grain boundaries for the metallic phase of $YBa_2Cu_3O_{7-\delta}$. Actually the holes can segregate around charged boundaries even if not metallic. These can be localized hole distributions. The generic phase diagram of the cuprates shows a wide variety of different behaviour at different temperatures and levels of doping [10, 11]. At zero doping the cuprates are all insulators, and below a few hundred kelvin they are also antiferromagnets (i.e. the electron spins on neighbouring copper ions point in opposite directions). However, when the doping is increased above a critical value (about 5%, although this varies from compound to compound), the antiferromagnetic state disappears and we enter the so-called underdoped region. As the doping is increased further, the superconducting region is reached. For $YBa_2Cu_3O_{7-\delta}$, the doping is closely related to the oxygen content. Here we examine two limits: $\delta = 0, 1$. When $\delta = 1$, this is an insulator, which can be approximately treated as an ionic solid. However, when $\delta = 0$, the phase is superconducting, and has mobile holes. The existence of holes can add more screening than in the insulator case. This is quite similar to the

two limits of semiconductors: the point defect limit and electron/hole limit. As the oxygen content changes from O_7 to O_6, the *c*-axis expands [12]. The lattice strain has a large effect on point defects [13]. Besides, the valence of chain copper ions decreases from +2 to +1 as the oxygen content is reduced. Both factors lead to a dramatic change of point defect formation energies in 123 compounds. Consequently, this will affect the intrinsic space charge.

It has been known since the early days of YBCO that doping with calcium is one way of adding more holes to the material. Divalent calcium is roughly the same size as trivalent yttrium and so readily replaces it. If a deficiency of holes causes grain boundaries to have weak coupling, then the critical current might be improved by doping calcium into grain boundaries. Note that if calcium is doped inside the bulk as well, the bulk T_c will be lowered. Therefore, doping calcium at the grain boundaries can both repair the transport properties of grain boundaries and keep the high T_c value of the bulk. Indeed, Hammerl *et al* [14] recently developed one beautiful process to increase the critical current density above 10^5 A cm^{-2} at temperatures near the boiling point of liquid nitrogen by doping Ca into only high-angle grain boundaries of YBCO. So, the current key issue is to improve the transport properties near low-angle [001] tilt grain boundaries, which are the main types of defects in polycrystalline YBCO wires and tapes [15–17]. For small-angle grain boundaries, Gurevich *et al* [18] argue that the critical current density dependence is mostly determined by the decrease of the current-carrying cross section by insulating dislocation cores and by progressive local suppression of the superconducting order parameter near grain boundaries as θ increases. However, space charge effects due to Schottky disorder are not considered in their model, although there exist clear space charge profiles in cuprate superconductors [19]. It is thus desirable to make some theoretical inputs for this topic, which can help to provide useful guides to find practical ways to improve the transport properties of grain boundaries in YBCO.

In this paper, first we construct a statistical thermodynamic model to study the origin and evolution of space charges due to the spectrum of point defect formation energies as a function of the variation of oxygen content in $YBa_2Cu_3O_{7-\delta}$. Then we develop one kinetically-limited model, including the effects of doping and solute segregation, to study the process of Ca doping upon low-angle tilt grain boundaries in YBCO and consequential influences on the space charge profile.

2. Space charge profile for the intrinsic and doping cases for 123 compounds

The simplest imperfection in a crystal lattice is a lattice vacancy, which is a missing atom or ion. Electrically neutral and structure-preserving groups of vacancies, known as Schottky defects, are required in compounds. No matter by what means a Schottky defect is made, it is necessary to expend a certain

amount of work per atom taken to the surface. Therefore, the energy of the crystal is increased. At a finite temperature, the average energy of formation of the group of Schottky defects determines the concentration of such point defects at equilibrium. For a multicomponent crystal, the difference in the energy of formation of various defects determines the nature of the space charge near the interfaces [5]. We calculated the point defect formation energies for both $YBa_2Cu_3O_6$ and $YBa_2Cu_3O_7$ by the Mott– Littleton approach [20, 21], which has been implemented in GULP codes [22]. The pair potentials of the shell model used in this study were developed by Baetzold for Y-123 for studying ionic and electronic (polaron) defects [23]. The calculated point defect formation energies are collected in table 1. The data for $YBa_2Cu_3O_7$ agree nicely with the previous results [23] using HADES III codes [24]. It can be seen from table 1 that there is a wide spectrum in the calculated formation energies of individual vacancies in the Schottky group for both $YBa_2Cu_3O_6$ and $YBa_2Cu_3O_7$. Thus, in principle there should be space charges near free surfaces at equilibrium or quenched in from high temperatures where ionic mobility is high enough to maintain equilibrium. A similar phenomenon is expected to occur near internal interfaces such as grain boundaries, but the situation is more complex than for free surfaces for at least two reasons. First of all, the spectrum of dopant formation energies may be different for the process of removing an ion from a site in the bulk crystal and placing it at a site in the grain boundary. Of course, at equilibrium the chemical potential of defects is the same throughout the crystal, but the local variations in concentration will be affected by different energies for excess species (i.e. the ions removed to form the vacancies and placed at surface or boundary sites) in different types of interfaces. The second complicating factor is that the local stoichiometry in the structural units (or individual dislocation cores) making up the boundary may be significantly different from that of the bulk in complex ionic crystals. Advanced transmission electron microscopy has been used recently to show that this is the case for grain boundaries in $SrTiO_3$ [25] and for twin boundaries in $BaTiO_3$ [26]. It is not entirely clear how such local chemistry at boundaries in complex oxides will affect the intrinsic space charges arising from the spectrum of defect formation energies in equilibrium groupings, e.g. Schottky defects. Therefore, we will restrict our detailed calculations of intrinsic space charge to free surfaces, but we expect the behaviour at grain boundaries to be at least qualitatively similar.

2.1. Intrinsic space charge at surfaces

2.1.1. Insulator case: $YBa_2Cu_3O_6$. For the sake of simplicity, we assume that the crystal has free surfaces at $x = 0$ and $2L$ and is of infinite extent in the y and z directions in studying intrinsic space charge problems, i.e. only containing free surfaces. As discussed above, the case of grain boundaries is more complex, but the calculations for free surfaces will provide some qualitative guide to the understanding of intrinsic space charges, i.e. those due to equilibrium Schottky defects at other interfaces too. The free energy per unit area of a slab-like disordered crystal of the thickness $2L$ is given by

$$F = \int [n_Y E_Y + n_{Ba} E_{Ba} + n_{Cu_c} E_{Cu_c} + n_{Cu_p} E_{Cu_p} + n_{O_p} E_{O_p} + n_{O_a} E_{O_a} + \tfrac{1}{2}\rho(x)\Phi(x)]\,dx - T S_{conf}, \quad (1)$$

where $\Phi(x)$ is the electrostatic potential, $\rho(x)$ is the local charge density, and n_Y, n_{Ba}, n_{Cuc}, n_{Cup}, n_{Op}, and n_{Oa} stand for the densities (per unit volume) of vacancies at yttrium, barium, chain copper, plane copper, plane oxygen, and apex oxygen sites, respectively. Note that the configurational entropy density S_{conf} is calculated as

$$\frac{\delta S_{conf}}{k} = \delta n_Y \ln\frac{N}{n_Y} + \delta n_{Ba} \ln\frac{2N}{n_{Ba}} + \delta n_{Cu_c} \ln\frac{N}{n_{Cu_c}} + \delta n_{Cu_p} \ln\frac{2N}{n_{Cu_p}} + \delta n_{O_p} \ln\frac{4N}{n_{O_p}} + \delta n_{O_a} \ln\frac{2N}{n_{O_a}}, \quad (2)$$

where N is the number of formula units per unit volume. This arises because we have neglected the effects of clustering and association (e.g. the formation of di-vacancies, etc) among the defects. The charge density $\rho(x)$ is given by

$$\rho(x) = e(2n_{O_p} + 2n_{O_a} - 3n_Y - 2n_{Ba} - n_{Cu_c} - 2n_{Cu_p}). \quad (3)$$

From $\delta F = 0$, the spatially-varying equilibrium concentrations are

$$\begin{aligned}
n_Y &= N \exp\left(-\frac{E_Y - 3e\Phi}{kT}\right),\\
n_{Ba} &= 2N \exp\left(-\frac{E_{Ba} - 2e\Phi}{kT}\right),\\
n_{Cu_c} &= N \exp\left(-\frac{E_{Cu_c} - e\Phi}{kT}\right),\\
n_{Cu_p} &= 2N \exp\left(-\frac{E_{Cu_p} - 2e\Phi}{kT}\right),\\
n_{O_p} &= 4N \exp\left(-\frac{E_{O_p} + 2e\Phi}{kT}\right),\\
n_{O_a} &= 2N \exp\left(-\frac{E_{O_a} + 2e\Phi}{kT}\right).
\end{aligned} \quad (4)$$

The electrostatic potential $\Phi(x)$ is obtained from Poisson's equation, which can be written using equations (3) and (4) as

$$\nabla^2\Phi(x) = \frac{-4\pi}{\epsilon}\rho(x)$$
$$= \frac{-4\pi eN}{\epsilon}\left[2\times 4\times \exp\left(-\frac{E_{O_p}+2e\Phi}{kT}\right)\right.$$
$$+2\times 2\times \exp\left(-\frac{E_{O_a}+2e\Phi}{kT}\right)$$
$$-3\times 1\times \exp\left(-\frac{E_Y-3e\Phi}{kT}\right)$$
$$-2\times 2\times \exp\left(-\frac{E_{Ba}-2e\Phi}{kT}\right)$$
$$-1\times 1\times \exp\left(-\frac{E_{Cu_c}-e\Phi}{kT}\right)$$
$$\left.-2\times 2\times \exp\left(-\frac{E_{Cu_p}-2e\Phi}{kT}\right)\right], \qquad (5)$$

where ϵ is the static relative permittivity (ϵ = 5.21), which is obtained by atomistic simulations using our shell model [27] with pair potential parameters from Baetzold [23]. We define the electrostatic potential to be zero at the surface, and the bulk potential Φ_∞ is defined as the potential for which ρ = 0. Therefore, letting the right-hand side (RHS) of equation (5) equal zero, the bulk potential Φ_∞ can be obtained, and the defects' concentrations in bulk can be calculated. We also define the Debye length κ [5–7] as

$$\kappa = \left(\frac{\epsilon kT}{8\pi e^2\sum_i(n_i q_i^2)}\right)^{\frac{1}{2}}, \qquad (6)$$

where n_i is the density of vacancies on sites of type i, and q_i is the charge of the vacancy.

If we scale the original length r by the Debye length κ, and define one new variable z as follows,

$$s = \frac{x}{\kappa},$$
$$z = \frac{(e\Phi - e\Phi_\infty)}{kT}, \qquad (7)$$

equation (5) can be rewritten as

$$\frac{(\mathrm{d}^2 z)}{(\mathrm{d}s^2)} = -\frac{1}{2}\left[2 \times 4 \times \exp\left(-\frac{E_{\mathrm{O_p}} + 2e\Phi_\infty}{kT}\right)\exp(-2z)\right.$$
$$+ 2 \times 2 \times \exp\left(-\frac{E_{\mathrm{O_a}} + 2e\Phi_\infty}{kT}\right)\exp(-2z)$$
$$- 3 \times 1 \times \exp\left(-\frac{E_{\mathrm{Y}} - 3e\Phi_\infty}{kT}\right)\exp(3z)$$
$$- 2 \times 2 \times \exp\left(-\frac{E_{\mathrm{Ba}} - 2e\Phi_\infty}{kT}\right)\exp(2z)$$
$$- 1 \times 1 \times \exp\left(-\frac{E_{\mathrm{Cu_c}} - e\Phi_\infty}{kT}\right)\exp(z)$$
$$\left. - 2 \times 2 \times \exp\left(-\frac{E_{\mathrm{Cu_p}} - 2e\Phi_\infty}{kT}\right)\exp(2z)\right]. \qquad (8)$$

The boundary conditions for a slab of thickness $2L$ are given by

$$s = 0, \qquad z = -\frac{e(\Phi_\infty)}{kT}, \qquad (9)$$

$$s = \frac{L}{\kappa}, \qquad z = \frac{e(\Phi_L - \Phi_\infty)}{kT}, \qquad (10)$$

where Φ_L is the potential at $x = L$. In this study, we assume that the thickness approaches infinity, which means that the grain boundary is qualitatively modelled by two surfaces 'back to back'. Under this condition Φ_L approaches Φ_∞. We solved equation (8) by conventional numerical integration techniques for several temperatures. The results are plotted in figure 1. Since there is no oxygen at chain sites for $YBa_2Cu_3O_6$, the chain copper is comparatively loosely bound inside the crystal. Based on the point defect energy calculations, it turns out that it costs the least energy to make such a copper vacancy (see table 1). Because the free energies of formation of the anion and cation vacancies differ, there exists a charged surface and a region of space charge of the opposite sign adjacent to the surface. For $YBa_2Cu_3O_6$, this leads to a positively charged surface and a region of negative space charge beneath the surface. Presumably this also would be the case for dislocations and grain boundaries.

Based on the point defect energies in $YBa_2Cu_3O_6$ (table 1), the Debye length κ and bulk potential Φ_∞ are tabulated in table 2 for various temperatures. As the temperature rises, the concentrations of point defects increase exponentially such that the Debye length becomes reduced at higher temperature. Next, let us consider the trend of bulk potential versus temperature. In the RHS of equation (5), it is seen that at lower temperature there is a bigger difference among $\exp(-\frac{E_{ION}}{kT})$. To balance this, a larger absolute value of the bulk potential relative to the surface is needed. Since this potential is positive, this expels holes from the surface. In other words, the positively charged surface can cause a serious depletion of the hole content there.

2.1.2. Metallic case: $YBa_2Cu_3O_7$. Compared with $YBa_2Cu_3O_6$, the defect energy 'spectrum' as calculated with the shell model with pair potential parameters from [23] is different for $YBa_2Cu_3O_7$

(see table 1). The similar comparison has also been discussed by Baetzold in studying point defects in $YBa_2Cu_3O_7$ and $YBa_2Cu_3O_{6.5}$ [23, 28]. Since the plane copper is coordinated with four oxygens, it is quite stable in the sense that more energy is needed to make a vacancy at the copper site in CuO_2 planes. Interestingly, our atomistic simulations show that the formation energy of oxygen vacancies in the CuO_2 plane is the lowest one in $YBa_2Cu_3O_7$. Another very important difference is the existence of screening by mobile holes in $YBa_2Cu_3O_7$, which is absent in $YBa_2Cu_3O_6$ because it is an insulator. In our atomistic simulations of the formation energy of point defects we ignore the explicit screening of defects by mobile holes. However, the screening by holes is included in the space charge calculations, assuming holes are localized on ion sites (but mobile by hopping between ions). Considering that the temperature of fabrication of $YBa_2Cu_3O_7$ is much higher than T_c, $YBa_2Cu_3O_7$ is in fact in a normal state. The Ioffe–Refel resistivity of $YBa_2Cu_3O_7$ at normal state is very large, about 0.1 mΩ cm, due to the small carrier concentration [29, 30]. Emery and Kivelson suggested that this type of exotic 'bad metal' can still be regarded as a quasiparticle insulator [31]. These observations encourage us to apply the classical approach to study the effects of band-bending on the hole's segregation near surfaces at fairly high temperature (above 600 K), at which $YBa_2Cu_3O_7$ remains in a metallic normal state.

Following a procedure similar to that used for $YBa_2Cu_3O_6$, but now including chain oxygen vacancies and localized (but mobile) holes, from $\delta F = 0$ the equilibrium concentrations are

$$
\begin{aligned}
n_{\mathrm{Y}} &= N \exp\left(-\frac{E_{\mathrm{Y}} - 3e\Phi}{kT}\right),\\
n_{\mathrm{Ba}} &= 2N \exp\left(-\frac{E_{\mathrm{Ba}} - 2e\Phi}{kT}\right),\\
n_{\mathrm{Cu_c}} &= N \exp\left(-\frac{E_{\mathrm{Cu_c}} - 2e\Phi}{kT}\right),\\
n_{\mathrm{Cu_p}} &= 2N \exp\left(-\frac{E_{\mathrm{Cu_p}} - 2e\Phi}{kT}\right),\\
n_{\mathrm{O_p}} &= 4N \exp\left(-\frac{E_{\mathrm{O_p}} + 2e\Phi}{kT}\right),\\
n_{\mathrm{O_a}} &= 2N \exp\left(-\frac{E_{\mathrm{O_a}} + 2e\Phi}{kT}\right),\\
n_{\mathrm{O_c}} &= N \exp\left(-\frac{E_{\mathrm{O_c}} + 2e\Phi}{kT}\right),
\end{aligned}
\qquad (11)
$$

where n_{Oc} stands for the density (per unit volume) of vacancies at chain oxygen sites. Since mobile holes are present in $YBa_2Cu_3O_7$, the charge density is given by

$$
\rho(x) = e(2n_{\mathrm{O_p}} + 2n_{\mathrm{O_a}} + 2n_{\mathrm{O_c}} - 3n_{\mathrm{Y}} - 2n_{\mathrm{Ba}} - n_{\mathrm{Cu_c}} - 2n_{\mathrm{Cu_p}} + n_{\mathrm{hole}}). \qquad (12)
$$

To calculate the bulk potential Φ_∞, we assume that the holes are bound to oxygen ions in the CuO_2 plane

such that the effective valence of oxygen changes from −2 to −1.75. Within this approximation, we compute the individual defect energy by the Mott–Littleton approach. Then by applying the charge neutrality constraint for the bulk, the bulk potential Φ_∞ is obtained. The resulting values of bulk potential and Debye length are tabulated in table 3.

Notice that when including the screening effect caused by mobile holes, the bulk potential is invariant. However, the Debye length changes dramatically because of the hole concentration. At the optimally doped case, there is around 0.2 holes per CuO_2 [10]. Therefore, the total hole content is about 0.4 per unit cell of $YBa_2Cu_3O_7$. We assume that the holes are localized, but can hop from site to site. Hence, the hole content at the position x with the electrostatic $\Phi(x)$ inside the slab is given as

$$n_{\text{hole}}(x) = N \cdot f_0 \times \exp \frac{-e(\Phi(x) - \Phi_\infty)}{kT}, \qquad (13)$$

where $N \cdot f_0$ is the density of holes at surfaces, determined by the following condition:

$$0.4 \times N \times V = \int \mathrm{d}A \int \mathrm{d}x\, N \cdot f_0 \times \exp \frac{-e(\Phi - \Phi_\infty)}{kT}, \quad (14)$$

where $\mathrm{d}A = \mathrm{d}y \times \mathrm{d}z$ is the area. After the same process as described in the previous section, the Poisson equation yields

$$\begin{aligned}\frac{(\mathrm{d}^2 z)}{(\mathrm{d}s^2)} = -\frac{1}{2}\Bigg[& 2 \times 4 \times \exp\left(-\frac{E_{\mathrm{O_p}} + 2e\Phi_\infty}{kT}\right)\exp(-2z) \\ & + 2 \times 2 \times \exp\left(-\frac{E_{\mathrm{O_a}} + 2e\Phi_\infty}{kT}\right)\exp(-2z) \\ & + 2 \times 1 \times \exp\left(-\frac{E_{\mathrm{O_c}} + 2e\Phi_\infty}{kT}\right)\exp(-2z) \\ & - 3 \times 1 \times \exp\left(-\frac{E_{\mathrm{Y}} - 3e\Phi_\infty}{kT}\right)\exp(3z) \\ & - 2 \times 2 \times \exp\left(-\frac{E_{\mathrm{Ba}} - 2e\Phi_\infty}{kT}\right)\exp(2z) \\ & - 2 \times 1 \times \exp\left(-\frac{E_{\mathrm{Cu_c}} - 2e\Phi_\infty}{kT}\right)\exp(2z) \\ & - 2 \times 2 \times \exp\left(-\frac{E_{\mathrm{Cu_p}} - 2e\Phi_\infty}{kT}\right)\exp(2z) \\ & + f_0 \times \exp(-z)\Bigg]. \end{aligned} \qquad (15)$$

In $YBa_2Cu_3O_7$, based on the shell model calculations of point defect energies, it turns out that it is much easier to create oxygen vacancies in the CuO_2 plane than any other type of vacancy (see table 1). The space charge profile is obtained by numerical solutions of equation (15) at several temperatures, which are plotted in figure 2. In our model, in contrast to $YBa_2Cu_3O_6$ (insulator), $YBa_2Cu_3O_7$ is a p-type superconductor,

containing mobile holes. Assume that the total hole content is 0.4 per unit cell; this makes the dominant contribution to the total charge density such that the total charge density is effectively constant over the temperature range of interest. As for the bulk potential relative to the surface calculated by the procedure described in the previous section, its value is determined by differences among the $\exp(-\frac{E_{ION}}{kT})$ terms. So, at higher temperature, a much smaller bulk potential is needed to keep the bulk neutral. As the total charge density is effectively constant, the Debye length is proportional to the square root of the temperature (see equation (6)). It is intrinsically different from the corresponding trend for $YBa_2Cu_3O_6$. Furthermore, note that the Debye length of O_7 is far shorter than that of O_6; the mobile hole provides strong screening of the charge at grain boundaries. We also computed the Thomas–Fermi screening length λ_{TF} by the following relation [32]:

$$\lambda_{TF} = \frac{\hbar}{e}\left(\frac{\epsilon}{4m_{hole}}\right)^{\frac{1}{2}}\left(\frac{\pi}{3 \times (0.4 \times N)}\right)^{\frac{1}{6}}, \qquad (16)$$

where m_{hole} is the effective mass of the hole, N is the number of $YBa_2Cu_3O_7$ unit cell per volume, and we assume that the total hole density is equal to $0.4 \times N$ for optimal doping. The calculated λ_{TF} is around 1 Å by taking $m_{hole} = m_{ele}$. It is interesting to note that both lengths, the Thomas–Fermi screening length λ_{TF} and the Debye length κ, are shorter that an interionic spacing. Because the holes are localized, the effective mobile hole density is expected to be only a small amount of the total density. In fact, κ and λ_{TF} are the lower limit of the effective screening length. The very short screening length can help to protect the superconducting properties inside the bulk from the influence of grain boundaries if the hole density of the grain boundaries corresponds to $YBa_2Cu_3O_7$. However, experiments have shown that the oxygen content at the grain boundaries is often less than that inside the bulk [2]. If the oxygen content is less than around $O_{6.45}$, from the calculation in the previous section it can be concluded that the Debye length will increase dramatically. It means that a large portion of the bulk near the boundary will be affected by the internal electric field caused by the space charge around the grain boundaries. This may be one reason for the vicinity of some grain boundaries not being a good superconductor.

2.2. Space charge of calcium-doped $YBa_2Cu_3O_7$

After the discovery of $YBa_2Cu_3O_7$, many types of ions have been chosen to dope into $YBa_2Cu_3O_7$ in search of new superconductors and to improve properties. Doping with Ca into [001] tilt grain boundaries of YBCO has been shown to increase the critical current density above 10^5 A cm^{-2} [14]. Our goal here is to study the segregation of calcium around small-angle tilt boundaries of Y-123 in order to aid the search for a more efficient approach for doping Ca. First, doping calcium in bulk is studied by shell model calculations to identify the energetically favourable reaction for doping. Second, the volume of solution of a Ca dopant atom is calculated. Third, the segregation of calcium is represented in terms of the segregation energy as a function of the angle around the core of edge dislocations in tilt boundaries, which can clarify the role of the elastic strain field. Finally, the space charge profile is studied by including extra holes due to dopants and

segregation of dopants due to the strain field.

2.2.1. Site preference. When Ca replaces Y, it is accompanied by a hole for the sake of charge neutrality. However, when substituting Ca for Ba, the charge remains balanced without changing the total hole content. Thus, it is important to know the circumstances when Ca doping yields Ca on Y or Ca on Ba sites. Here, we mainly focus on the dissolution of divalent Ca^{2+}, which can be represented by the following defect reactions, depending on which sublattice Ca^{2+} chooses and what kind of charge compensation is involved. The parameter *m* is chosen to characterize the dopant concentration in the YBCO.

$$CaO + mYBa_2Cu_3O_7 \rightarrow mY(Ba_{\frac{2m-1}{2m}}Ca_{\frac{1}{2m}})_2Cu_3O_7 + BaO; \quad (17)$$

$$2CaO + 2mYBa_2Cu_3O_7 + \tfrac{1}{2}O_2 \rightarrow 2m(Y_{\frac{m-1}{m}}Ca_{\frac{1}{m}})(BaO)_2(Cu^{3+}O)_{\frac{1}{2m}}(CuO)_{\frac{2m-1}{2m}}(CuO_2)_2 + Y_2O_3; \quad (18)$$

$$2CaO + 2mYBa_2Cu_3O_7 + \tfrac{1}{2}O_2 \rightarrow 2m(Y_{\frac{m-1}{m}}Ca_{\frac{1}{m}})(BaO)_2(CuO)(Cu^{3+}O_2)_{\frac{1}{2m}}(CuO_2)_{\frac{4m-1}{2m}} + Y_2O_3. \quad (19)$$

The first case, equation (17), is homovalent substitution. Simply, barium is replaced by calcium. However, yttrium is replaced in the last two reactions (equations (18) and (19)). These two reactions are aliovalent substitutions, in which it is very important to identify the mechanism of charge compensation. In reaction (18), a hole is created in the CuO chain to make the whole system charge neutral. Assuming that the hole is trapped at a copper site, the valence of one copper at a chain site increases by approximately one. In reaction (19), we assume that the extra hole is in the CuO_2 plane, such that the valence of one copper in the plane increases by one. All the calculations are done by assuming infinite dilution of dopants. When the valence of copper changes, the corresponding interatomic pair potentials are scaled based on a simple radius scheme [13]. GULP was used to compute the defect energies. The calculated energies of solution (per calcium) are listed in table 4. Previous studies on bipolaron binding energies have shown that the hole is more likely to be localized on copper sites than oxygen sites in the CuO_2 planes [23]. In our studies, the hole content is tuned by the dopant, calcium. The calculations suggest that it is most energetically favourable to substitute a calcium ion at an yttrium site, together with the creation of one hole in the CuO_2 plane. This agrees very well with experimental measurements [14].

2.2.2. Volume of solution for doping alkaline earth ion (AE^{2+}) at the Y^{3+} site. Doping Ca in grain boundaries of YBCO can improve the transport properties significantly since more holes are created near the grain boundaries. The strong elastic strain field around the grain boundaries has an important role in the segregation of dopants. The disruption of the lattice by a point defect, such as a dopant atom like Ca^{2+}

substituting for Y^{3+} in YBCO, gives rise to forces on the surrounding lattice atoms which, in turn, give rise to a displacement field in the lattice around the defect. The interaction between the defect displacement field and the stress fields of other defects, such as dislocations, or applied stress fields, alters the energy of the defect [33–35] and causes defect segregation. The effects of the forces on the lattice due to the point defect can be described by means of force multipoles [33], which, together with the Green tensor function of the matrix of the perfect crystal, can be used to calculate the resulting displacement field caused by the defect in the crystal. In this section, we use numerical shell model calculations with GULP to estimate the strength of the elastic force dipole for the point defects (dopants). Then in the next section we apply anisotropic continuum elasticity to describe the stress field due to an edge dislocation; finally we use continuum elasticity theory to compute the elastic interaction between the dopant atom and the dislocation. Such methods have been shown to give good agreement with direct numerical calculations of the interaction between external pressure and vacancies in simple crystals such as van der Waals bonded rare gas crystals (see appendix 3 in [34]).

To study the segregation of calcium around tilt grain boundaries, it is necessary to have the volume of solution to compute the contribution to the binding energy of Ca^{2+} at the grain boundaries due to interactions with the strain field of edge dislocations in the boundaries. In the force–dipole approximation, the difference between the energy to form the defect in a crystal containing a strain field ϵ_{ij} (either from an applied stress or from the stress field of another defect) and the energy in the strain-free crystal is given as

$$E_{\text{int}} = -a_{ij}\epsilon_{ij}, \qquad (20)$$

where the Einstein summation convention for repeated indices is used and the coefficients a_{ij} characterize the strength of the defect forces on the lattice. The effective body force, f, which the defect exerts on the lattice, is

$$f_i = -a_{ij}\frac{\partial}{\partial x_j}\delta(r), \qquad (21)$$

where $\delta(r)$ is the Dirac delta function. These three force components represent three orthogonal 'double forces without moment' and are sometimes called 'force dipoles'. The values of a_{ij}, which have the unit of energy, must be obtained from experiment or numerical simulations. For a defect with spherical symmetry in an elastically isotropic matrix,

$$a_{ij} = a\delta_{ij}, \qquad (22)$$

where δ_{ij} is the Kronecker δ (=1, if $i = j$; =0, if $i \neq j$), and

$$a = B\Omega, \qquad (23)$$

where Ω is the volume change produced by the formation of the defect in a finite crystal and B is the bulk

modulus [35]. Thus from equation (20) we obtain

$$E_{\text{int}} = -B\Omega(\epsilon_{11} + \epsilon_{22} + \epsilon_{33}) = P\Omega, \qquad (24)$$

where P is the hydrostatic component of pressure at the defect, produced by external forces or other defects.

In the case of a defect with orthorhombic symmetry, equation (20) yields

$$E_{\text{int}} = -[a_{11}\epsilon_{11} + a_{22}\epsilon_{22} + a_{33}\epsilon_{33}]. \qquad (25)$$

Clearly, it is necessary to evaluate E_{int} for three uniaxial strain cases. For strain along the a-axis ($\epsilon_{11} \neq 0; \epsilon_{22} = \epsilon_{33} = 0$), we have

$$a_{11} = -\frac{E_{\text{int}}}{\epsilon_{11}}, \qquad (26)$$

where E_{int} is evaluated from numerical simulation by GULP. Using a generalized Hooke's law in the form of elastic compliances, $S_{ij,}$ we obtain by choosing the crystal axes as principal ones

$$\begin{aligned} \epsilon_{11} &= S_{11}\sigma_{11} + S_{12}\sigma_{22} + S_{13}\sigma_{33}, \\ \epsilon_{22} &= S_{12}\sigma_{11} + S_{22}\sigma_{22} + S_{23}\sigma_{33}, \\ \epsilon_{33} &= S_{13}\sigma_{11} + S_{23}\sigma_{22} + S_{33}\sigma_{33}. \end{aligned} \qquad (27)$$

Hence, the components of the volume of formation of the dopants are given as

$$\begin{aligned} \Omega_{11} &= S_{11}a_{11} + S_{12}a_{22} + S_{13}a_{33}, \\ \Omega_{22} &= S_{12}a_{11} + S_{22}a_{22} + S_{23}a_{33}, \\ \Omega_{33} &= S_{13}a_{11} + S_{23}a_{22} + S_{33}a_{33}. \end{aligned} \qquad (28)$$

The calculated components of the volume of solution for various divalent ions (AE^{2+}) at the Y^{3+} site of $YBa_2Cu_3O_7$ are plotted in figure 3. Considering the trend across the series of AE^{2+}, the ion size plays the important role in the stress effects caused by doping AE^{2+} at Y^{3+}. The point defect for doping AE^{2+} at the Y^{3+} site carries one negative charge. This strongly repels the surrounding oxygen ions to make the sign of the volume of solution positive for AE ions whose radius is similar to or larger than that of Y^{3+} (1.02 Å). Note that the short range repulsion between the AE and the surrounding oxygen ions becomes larger with increasing AE ion radius; it is expected that the volume of solution increases with AE ion radius. However, for an AE ion with a larger radius, the polarization of the lattice around the solute which helps to lower the defect's energy by polarizing electron 'clouds' also depends on the distortion of the lattice by the AE ion and thus

contributes to the volume of formation. Therefore, because of these competing effects the volume of formation ends up with a 'saturation-like' curve.

2.2.3.Dislocation stress fields in Y-123. The grain boundaries of importance in coated conductors are low-angle [001] tilt boundaries. Thus they can be considered as an array of isolated edge dislocations. We observe that the elasticity in $YBa_2Cu_3O_7$ is not far different between the *a*- and *b*-axis ((C_{xx} - C_{yy})/C_{yy} ~ 0.082), so this orthorhombic crystal can be approximated by a hexagonal one, which is motivated by the existence of closed-form expressions for the stress fields in the case of anisotropic elasticity in hexagonal crystals. Here we average the elastic constants of orthorhombic symmetry into those permitted by hexagonal symmetry by taking an arithmetical average of the corresponding elastic moduli. The geometry of the dislocations in [001] tilt boundaries in Y-123 is like prismatic slip in hexagonal crystals. The Burger's vector lies in the basal plane ($\frac{a}{3}\langle 1\bar{2}10\rangle$), while the dislocation line runs along the hexad axis. The prismatic planes are $\langle\bar{1}010\rangle$. Following [36], on account of the basal plane isotropy, the stress field is given by

$$\sigma_{xx} = \frac{K_1 \cdot b \cdot y \cdot (3x^2 + y^2)}{2\pi \cdot (x^2 + y^2)^2}, \qquad (29)$$

$$\sigma_{yy} = \frac{-K_1 \cdot b \cdot y \cdot (x^2 - y^2)}{2\pi \cdot (x^2 + y^2)^2}, \qquad (30)$$

$$\sigma_{zz} = -\frac{s_{xz}}{s_{zz}} \cdot (\sigma_{xx} + \sigma_{yy}), \qquad (31)$$

where *s* is the elastic compliance modulus, and

$$K_1 = \frac{s_{zz}}{[2 \cdot s_{xx}s_{zz} - s_{xz}^2]}.$$

(Note: The formula of K_1 on page 192 of [36] has one misprint.)

Small-angle (usually less than 5°) grain boundaries can be considered as an array of isolated dislocations. The separation between dislocations is around $d \cong \frac{b}{\theta}$. If we assume that a superposition approximation can be applied here, the total stress field can be written as

$$\sigma_{ii}^{\text{total}} = \sum_{n=-2,\ldots,+2} \sigma_{ii}(y + nd). \qquad (32)$$

When doping calcium at yttrium sites, the non-zero tensional elements of the 'volume of solution' will

interact with the stress field. Neglecting the effect of the solute atom on the local elastic moduli, the segregation energy of calcium can be written as

$$E_{\text{seg}} = \sum_{i=x,y,z} \sigma_{ii}^{\text{total}} \Omega_{ii}. \qquad (33)$$

In the previous section, we calculated the energy for doping calcium at yttrium sites inside a stress free bulk Y-123. Here we computed the segregation energy for calcium due to the stress field around very small-angle (usually less than 5°) tilt boundaries, which is plotted in figure 4. Since our region of interest is at a small distance from the dislocation cores, there exist possible errors in using linear elasticity theory here, and our results are probably overestimated. However, the relative energy differences are more important than absolute values. In figure 4, the calculations show that calcium segregation is expected to the tensile stress region due to the positive sign of the volume of formation. This will affect the distribution of mobile holes around the grain boundaries. We will study this further in the following section for general grain boundaries.

2.2.4. Effects on space charge due to the segregation of calcium near grain boundaries. It has been noted [37] that edge dislocations could act as sources and sinks for vacancies such that space charges would appear also in the regions near dislocation cores. The modelling of space charges around dislocation cores is more difficult than our treatment of the intrinsic space charges at free surfaces from the difference in formation energy of equilibrium point defects, if for no other reason than the fact that the difference in the energy required for the creation of point defects by removing ions from the bulk and placing them in the dislocation core, it is not likely to be quite the same as that for free surfaces. However, there is also likely to be an alteration of the space charge by dopants and their accompanying holes if the dopants tend to segregate to the dislocations. In the previous section 2.2.3 it was shown that there is a strong attraction of the AE^{2+} dopants, i.e. Ca, Sr, and Ba, to the tensile regions of isolated edge dislocations in low-angle grain boundaries and a repulsion from the compressive regions. We will illustrate some of the effects of such dopant segregation on the space charges by an idealized planar grain boundary which consists of joining together two free surfaces with their associated point defect space charges, together with Ca^{2+} dopants and accompanying holes which have segregated in the stress fields of the boundary. We assume that the dopant atoms are attracted to or repelled from region along the boundary by the elastic fields which decay going away from the boundary. The results of this calculation will illustrate the interplay between dopant segregation and point defect induced by space charges.

From previous thermodynamic calculations we know that the hole density changes with the content of doped calcium. Consequently, the Debye length varies with Ca concentration. Note that the defect created by replacing Y^{3+} with Ca^{2+} carries one negative charge. Assuming that the total number of Ca^{2+} is conserved, after solving the distribution of charged particles in an electrostatic field caused by space charges, the defect density n_{Ca} at

the position of x with the electrostatic $\Phi(x)$ away from the boundary plane is given as

$$n_{\mathrm{Ca}} = N \cdot f_{\mathrm{Ca}} \times \exp \frac{e(\Phi - \Phi_{\infty})}{kT}, \qquad (34)$$

where $N \cdot f_{\mathrm{Ca}}$ is the density of calcium ions at surfaces determined by the following condition

$$N \cdot n_{\mathrm{doping}}^{\mathrm{Ca}} \cdot V = \int \mathrm{d}A \int \mathrm{d}x\, N \cdot f_{\mathrm{Ca}} \cdot \exp\left(\frac{e(\Phi - \Phi_{\infty})}{kT}\right), \qquad (35)$$

where n_{doping}^{Ca} is the total concentration of doped calciums. Since each Ca^{2+} is accompanied by one mobile hole, the density of holes near surfaces ($N \cdot f_0$) is determined by the following condition (assuming that the total number of holes is conserved):

$$(0.4+n_{\mathrm{doping}}^{\mathrm{Ca}})N \times V = \int \mathrm{d}A \int \mathrm{d}x\, N \cdot f_0 \cdot \exp \frac{-e(\Phi - \Phi_{\infty})}{kT}. \qquad (36)$$

Note that we extend our studies to general grain boundaries here based on understanding the divalent dopants' interaction with the stress field of small-angle tilt boundaries. As there can be a significant strain field in the grain boundary region, originating from size mismatch between solute and matrix atoms, dislocations, etc, a strain energy term should be included in the studies of Ca doping because the strain field due to dislocations at grain boundaries can substantially affect the segregation of Ca. We ignore the elastic interactions with the boundaries of the charged vacancies, and approximate the effect of the stress field of the boundary by an elastic term of the calcium by the same form used in [8]:

$$\begin{aligned} U_{\mathrm{elastic}} &= U_0\left(1 - \left(\frac{s \cdot \kappa}{d}\right)^n\right), \qquad s \cdot \kappa \leqslant 2d; \\ &= 0, \qquad s \cdot \kappa > 2d, \end{aligned} \qquad (37)$$

where U_0 is the binding energy near the dislocation core. We choose n = 2, and d is about two lattice parameters along the b-axis. This is consistent with the periodicity of the structural units proposed in the coincidence models of grain boundary structures [38]. The calculations in the previous section indicated that the volume of solution for doping calcium at yttrium sites is positive. Hence, a positive sign of U_0 means in the compression region which repels Ca, while a negative sign of U_0 means in the tensile region which attracts Ca. The charge density is now given by

$$\begin{aligned} \rho(x) = e(&2n_{\mathrm{O_p}} + 2n_{\mathrm{O_a}} + 2n_{\mathrm{O_c}} - 3n_{\mathrm{Y}} - 2n_{\mathrm{Ba}} - n_{\mathrm{Cu_c}} - 2n_{\mathrm{Cu_p}} \\ &+ n_{\mathrm{hole}} - n_{\mathrm{Ca}}). \end{aligned} \qquad (38)$$

Following the same process as in the previous section, the Poisson equation can be rewritten as

$$\frac{(\mathrm{d}^2 z)}{(\mathrm{d}s^2)} = -\frac{1}{2}\left[2\times 4\times \exp\left(-\frac{E_{O_p}+2e\Phi_\infty}{kT}\right)\exp(-2z)\right.$$
$$+2\times 2\times \exp\left(-\frac{E_{O_a}+2e\Phi_\infty}{kT}\right)\exp(-2z)$$
$$+2\times 1\times \exp\left(-\frac{E_{O_c}+2e\Phi_\infty}{kT}\right)\exp(-2z)$$
$$-3\times 1\times \exp\left(-\frac{E_Y-3e\Phi_\infty}{kT}\right)\exp(3z)$$
$$-2\times 2\times \exp\left(-\frac{E_{Ba}-2e\Phi_\infty}{kT}\right)\exp(2z)$$
$$-2\times 1\times \exp\left(-\frac{E_{Cu_c}-2e\Phi_\infty}{kT}\right)\exp(2z)$$
$$-2\times 2\times \exp\left(-\frac{E_{Cu_p}-2e\Phi_\infty}{kT}\right)\exp(2z)$$
$$\left.+f_0\times\exp(-z)-f_{Ca}\times\exp\left(z-\frac{U_{elastic}}{kT}\right)\right]. \qquad (39)$$

When calcium is doped in YBCO, the process is often designed so that calcium diffuses into grain boundaries first. However, it is difficult to estimate the amount of calcium at the grain boundaries during the deposition process. In this section, we assume that the hole density and the amount of calcium near the grain boundaries are 0.6 and 0.08 per unit volume, respectively. Furthermore, the elastic binding energy of calcium is chosen to include both compression and tension regions: U_0 = (−6, −4, −2, 0, 2, 4, 6)kT . This is shown in figure 5 for an idealized boundary in $YBa_2Cu_3O_7$. As discussed in the previous section, the grain boundaries in O_7 may be negatively charged because of the intrinsic space charges due to point defects. It should also be stressed that calcium is doped at yttrium sites, such that this site has one negative charge accompanied by making holes at CuO_2 planes. Therefore, the screening length becomes even shorter than that of pure $YBa_2Cu_3O_7$. If the calcium is pushed away from the grain boundaries, the space charge remains almost the same (somehow little dependent on repulsive energy). However, on the other hand, if the calcium is attracted by the grain boundaries, extra negative charge will accumulate around the grain boundaries such that the space charge's profile is significantly adjusted. This can strongly perturb the distribution of mobile hole density around the grain boundaries. The stress field around the grain boundaries is also so strong (around 10^2 GPa based on our calculated elastic properties of YBCO) that it significantly affects the surrounding oxygen content and ordering [13]. If the oxygen content is close to O_6, the grain boundaries are possibly positively charged, and the large Debye length leads to a larger portion of the bulk being exposed to the influence of the grain boundaries. Under such circumstances, doping with calcium not only neutralizes (by the intrinsic negative charge of Ca_Y^{-1}) the charged boundaries, but also increases the density of mobile holes to screen the charged boundaries. Therefore, the bad low-angle tilt boundaries are 'cured' by doping calcium.

3. Conclusions

We have systematically studied the space charge profile for $YBa_2Cu_3O_6$, $YBa_2Cu_3O_7$, and Ca-doped cases. The intrinsic space charge is strongly dependent on the oxygen content of $YBa_2Cu_3O_{7-\delta}$, which is determined by the annealing temperature and oxygen partial pressure. For $YBa_2Cu_3O_6$, the chain copper is loosely bound with neighbouring two oxygens; therefore it is comparatively easier to create vacancies at copper chain sites for O_6. Hence, the grain boundaries are possibly positively charged. On the other hand, the calculations show that it requires less energy to make vacancies at oxygen sites for O_7. Consequently, it was seen that there exists a dramatic change in the nature of the space charge in going from O_6 to O_7. It is interesting to note that the origin of the screening in going from O_6 to O_7 is completely different. For O_6 it is the thermal activated vacancies, while for O_7 it is the mobile holes. This is very similar to the two screening mechanisms in semiconductors: one is intrinsic, the other is free carriers due to doped impurities. In addition, we have carried out studies of the segregation of calcium at tilt grain boundaries in the Y-123 compound. By comparing the calculated heat of solution for various doping mechanisms, we have found that the most energetically favourable defect reaction is that of doping calcium at yttrium sites accompanied by creating one hole in the CuO_2 plane per Ca ion. This conclusion is valid for the reaction in the bulk, which agrees with previous experimental measurements [14]. To study the segregation of calcium at tilt boundaries, the volume of formation is needed in order to estimate the binding energy to the elastic strain field which arises from the grain boundary dislocations. We computed this for the doping series of alkaline earths at yttrium sites. After including the strain field contribution, the segregation energy of calcium at small-angle tilt boundaries is obtained. The theoretical results suggest that more calcium is expected in the tensile regions around tilt grain boundaries. For the calcium-doped $YBa_2Cu_3O_{7-\delta}$ case, our calculations indicate that Y^{3+} ions are replaced by Ca^{2+} ions, accompanied by creating holes in the CuO_2 plane. The increase of hole content strongly enhances the screening effect by mobile holes. The strong screening effect (much shorter screening length) helps to decrease the area of influence of the grain boundaries. Besides, the segregation of calcium is strongly determined by the strain field. More calcium segregation is expected in tensile stress regions. Since the calcium is doped at yttrium sites, it has one negative charge. Therefore, the segregation of calcium causes extra negative defects to approach the grain boundaries such that the potential decreases quite significantly. Consequently, the hole content near the grain boundaries increases, thus helping to screen out the effect of disorder at the boundary. In summary, the nature of the space charge is closely related to the oxygen content. Doping calcium at small-angle tilt grain boundaries of YBCO leads to an increase of J_c through increasing the hole content, enhancing negative potential regions due to the segregation of calcium, and helping to passivate disorder at the boundary.

Acknowledgments

HBS is grateful for Chinatsu Maeda's kind assistance in preparing the manuscript. The work at

Brookhaven National Laboratory was performed under the auspices of the Division of Materials Sciences, Office of Science, US Department of Energy under contract No. DE-AC-02-98CH10886.

Note added. After submission of this manuscript, reference [39] reported the experimental measurement of potential curves near [001] tilt boundaries for both $YBa_2Cu_3O_{7-\delta}$ and Ca-doped $YBa_2Cu_3O_{7-\delta}$. In particular, the curves in figure 2 of [39] were nicely predicted by figures 2 and 5 in this manuscript. (Indeed, the main body of this manuscript has been already completed as chapter 6 of [27]. Figures 6.2 and 6.3 of [27] are in fact plotted here as figures 2 and 5.)

References

[1] Hilgenkamp H and Mannhart J 2002 *Rev. Mod. Phys.* **74** 485

[2] Dimos D, Chaudhari P and Mannhart J 1990 *Phys. Rev.* B **41** 4038

[3] Dimos D, Chaudhari P, Mannhart J and Legoues F K 1988 *Phys. Rev. Lett.* **61** 219

[4] Kung H, Hirth J P, Foltyn S R, Arendt P N, Jia Q X and Maley M P 2001 *Phil. Mag. Lett.* **81** 85

[5] Frenkel J 1946 *Kinetic Theory of Liquids* (Oxford: Oxford University Press)

[6] Lehovec K 1953 *J. Chem. Phys.* **21** 1123

[7] Kliewer K L and Koehler J S 1965 *Phys. Rev.* **140** A1226

[8] Yan M F, Cannon R M and Bowen H K 1983 *J. Appl. Phys.* **54** 764

[9] Yan M F, Cannon R M and Bowen H K 1983 *J. Appl. Phys.* **54** 779

[10] Zhang H B and Sato H S 1993 *Phys. Rev. Lett.* **70** 1697

[11] Tallon J L, Bernhard C, Shaked H, Hitterman R Land Jorgensen J D 1995 *Phys. Rev.* B **51** 12911

[12] Cava R J, Batlogg B, Chen C H, Rietman E A, Zahurak S M and Werder D 1987 *Nature* **329** 423

[13] Su H B, Welch D O and Wong-Ng W 2004 *Phys. Rev.* B **70** 054517

[14] Hammerl G, Schmehl A, Schulz R R, Goetz B, Bielefeldt H, Schneider C W, Hilgenkamp H and Mannhart J 2000 *Nature* **407** 162

[15] Guth K, Krebs H U, Freyhardt H C and Jooss C 2001 *Phys. Rev.* B **6414** 140508

[16] Durrell J H, Hogg M J, Kahlmann F, Barber Z H, Blamire M G and Evetts J E 2003 *Phys. Rev. Lett.* **90** 247006

[17] Foltyn S R, Arendt P N, Jia Q X, Wang H, MacManus-Driscoll J L, Kreiskott S, DePaula R F, Stan L, Groves J R and Dowden P C 2003 *Appl. Phys. Lett.* **82** 4519

[18] Gurevich A and Pashitskii E A 1998 *Phys. Rev.* B **57** 13878

[19] Schofield M A, Wu L and Zhu Y 2003 *Phys. Rev.* B **67** 224512

[20] Mott N F and Littleton M J 1938 *Trans. Faraday Soc.* **34** 485

[21] Mott N F and Gurney R W 1948 *Electronic Processes in Ionic Crystals* (Oxford: Oxford University Press)

[22] Gale J D 1997 *J. Chem. Soc. Faraday Trans.* **93** 629

[23] Baetzold R C 1988 *Phys. Rev.* B **38** 11304

[24] Norgett M J 1974 *Atomic Energy Research Establishment, Report* No R7650, Harwell, England

[25] McGibbon M M, Browning N D, Chisholm M F, McGibbon A J, Pennycook S J, Ravikumar V and Dravid V P 1994 *Science* **266** 102

[26] Jia C L and Urban K 2004 *Science* **303** 2001

[27] Su H B 2002 *PhD Thesis* SUNY at Stony Brook

[28] Baetzold R C 1991 *Physica* C **181** 252

[29] Orenstein J, Thomas G A, Millis A J, Cooper S L, Rapkine D H, Timusk T, Schneemeyer L F and Waszczak J V 1990 *Phys. Rev.* B **42** 6342

[30] Gunnarsson O, Calandra M and Han J E 2003 *Rev. Mod. Phys.* **75** 1085

[31] Emery V J and Kivelson S A 1995 *Phys. Rev. Lett.* **74** 3253

[32] Kittel C 1996 *Introduction to Solid State Physics* 7th edn (New York: Wiley)

[33] Teodosiu C 1982 *Elastic Models of Crystal Defects* (Berlin: Springer)

[34] Girifalco L A and Welch D O 1967 *Point Defects and Diffusion in Strained Metals* (London: Gordon and Breach)

[35] Eshelby J D 1956 *Solid State Physics* vol 3 (NY: Academic Press) pp 79–144

[36] Steeds J W 1973 *Introduction to Anisotropic Elasticity of Dislocations* (Oxford: Clarendon)

[37] Eshelby J D, Newey C W A, Pratt P Land Lidiard A B 1958 *Phil. Mag.* **3** 75

[38] Gleiter H and Chalmers B 1972 *Prog. Mater. Sci.* **16** 1

[39] Schofield M A, Beleggia M, Zhu Y M, Guth K and Jooss C 2004 *Phys. Rev. Lett.* **92** 195502

List of Tables

List of Figures

	$YBa_2Cu_3O_6$	$YBa_2Cu_3O_7$
E(Y)	14.42	12.71
E(Ba)	4.06	4.25
E(Cu-chain)	0.96	4.23
E(Cu-plane)	6.92	5.68
E(O-plane)	3.47	3.56
E(O-chain)		4.22
E(O-apex)	6.85	4.48

Table 1.

T (K)	$\frac{e\Phi_{\infty}}{kT}$	κ (m)
350	−27.42	44.34
400	−23.81	0.93
600	−15.61	1.83×10^{-4}
1000	−9.28	2.49×10^{-7}

Table 2.

T (K)	$\frac{e\Phi_{\infty}}{kT}$	κ (m)
600	3.55	1.58×10^{-11}
800	2.76	1.82×10^{-11}
1000	2.16	2.04×10^{-11}

Table 3.

Reaction (17)	3.14
Reaction (18)	2.99
Reaction (19)	1.02

Table 4.

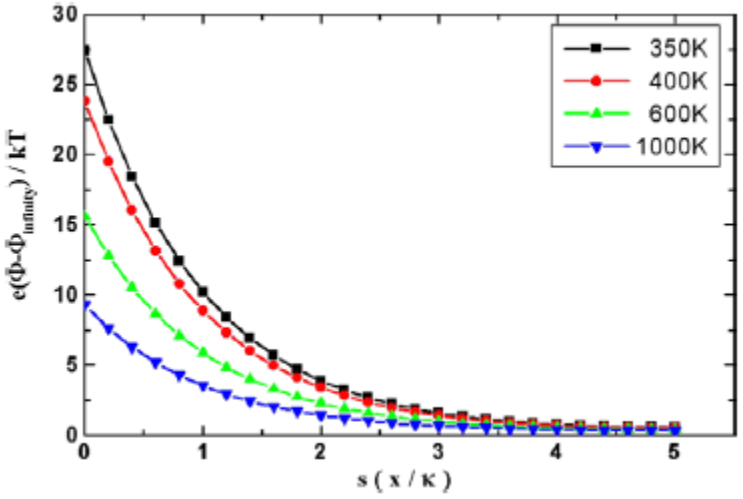
350K
400K
600K
1000K
e(Φ-Φinfinity) / kT
s (x / κ)
0
5
10
15
20
25
30
0
1
2
3
4
5

Fig. 1.

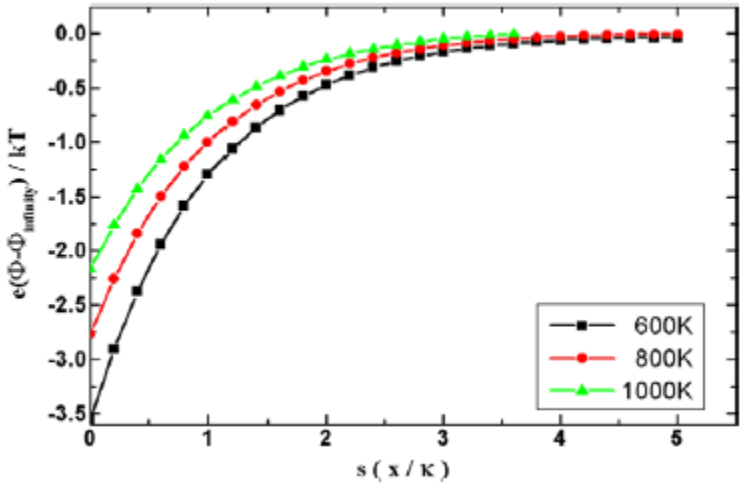
0.0
-0.5
-1.0
-1.5
-2.0
-2.5
-3.0
-3.5
0
1
2
3
4
5
e(Φ-Φinfinity) / kT
s (x / κ)
600K
800K
1000K

Fig. 2.

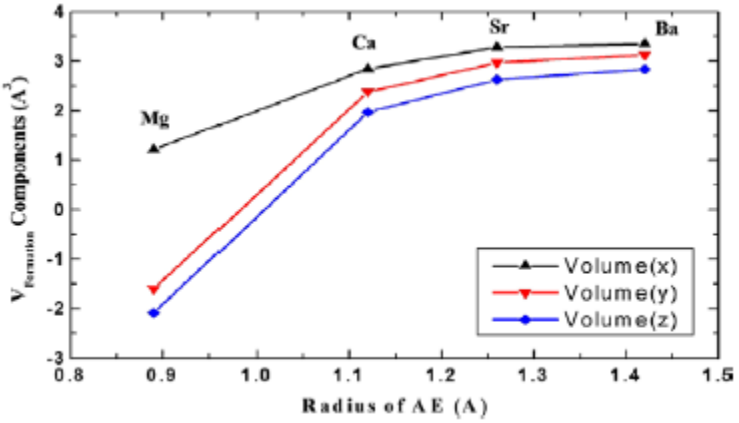
Mg
Ca
Sr
Ba
Volume(x)
Volume(y)
Volume(z)
Radius of AE (A)
Components (A^3)

Fig. 3.

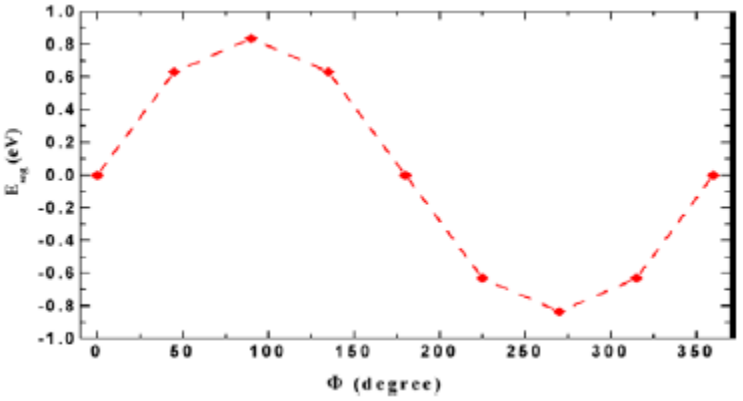
1.0
0.8
0.6
0.4
0.2
0.0
-0.2
-0.4
-0.6
-0.8
-1.0
E_xc (eV)
0
50
100
150
200
250
300
350
Φ (degree)

Fig. 4.

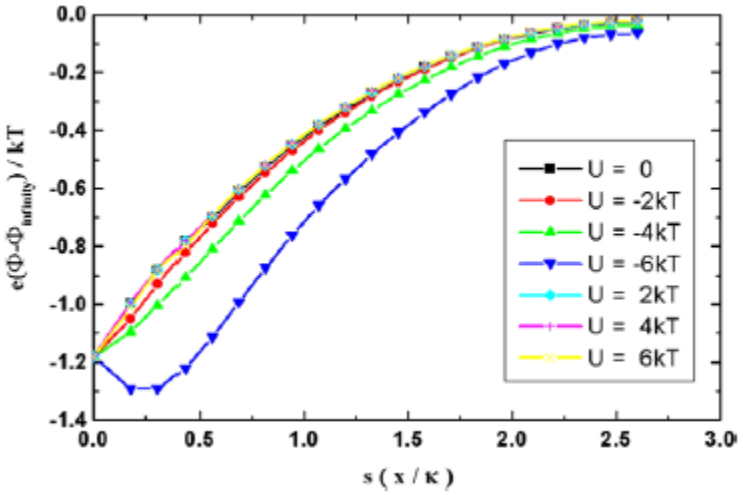
0.0
-0.2
-0.4
-0.6
-0.8
-1.0
-1.2
-1.4
0.0
0.5
1.0
1.5
2.0
2.5
3.0
e(Φ-Φinfinity) / kT
s (x / κ)
U = 0
U = -2kT
U = -4kT
U = -6kT
U = 2kT
U = 4kT
U = 6kT

Fig. 5.